

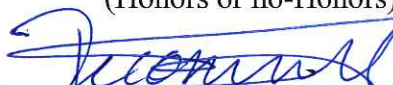
Determination and Simulation of Kinematic Parameters in the Qweak Experiment

A thesis submitted in partial fulfillment of the requirement
for the degree of Bachelor of Science in Physics from
The College of William and Mary

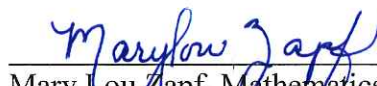
by

Rachel Charlotte Taverner

Accepted for Honors
(Honors or no-Honors)


Wouter Deconinck, Director


Henry Krakauer, Physics


Mary Lou Zapf, Mathematics

Williamsburg, VA
April 23, 2014

Determination and Simulation of Kinematic Parameters in the Qweak Experiment

Rachel Taverner

23 April 2014

Abstract

The Qweak Experiment aims to measure the weak charge of the proton. In order to obtain the required level of precision in the final result, we must calculate corrections to the momentum transfer, Q^2 , in the scattering event. We simulate the experiment in GEANT4 and compare the simulations to the experimental data. In my project, I was responsible for creating comparison plots for Q^2 , the scattering angle, θ , and the scattered energy, E' . We found that E' had some major discrepancies between experiment and simulation. After verifying that the simulations were implementing energy loss processes properly, we found that E' shows an octant-dependence consistent with a tilt to the rotator holding the vertical drift chambers.

1 Introduction

The Standard Model is currently the best theory in particle physics that describes the behavior of the universe. It models three of the four fundamental forces in the universe: the electromagnetic force, the strong nuclear force and the weak nuclear force, but does not incorporate the gravitational force. The model describes groups of fundamental particles, like quarks and leptons, and the particles that mediate the forces in the universe, the bosons. The familiar arrangement of the fundamental particles is shown in Figure 1, with the force-mediating bosons shown on the right, in red. The Standard Model also includes many measurable parameters, one of which is the weak mixing angle, θ_W , which is closely related to the weak nuclear interaction.

The two forces that we are most concerned with in my research are the electromagnetic force, which is mediated by the photon, and the weak interaction, which is mediated by either a Z or W^\pm

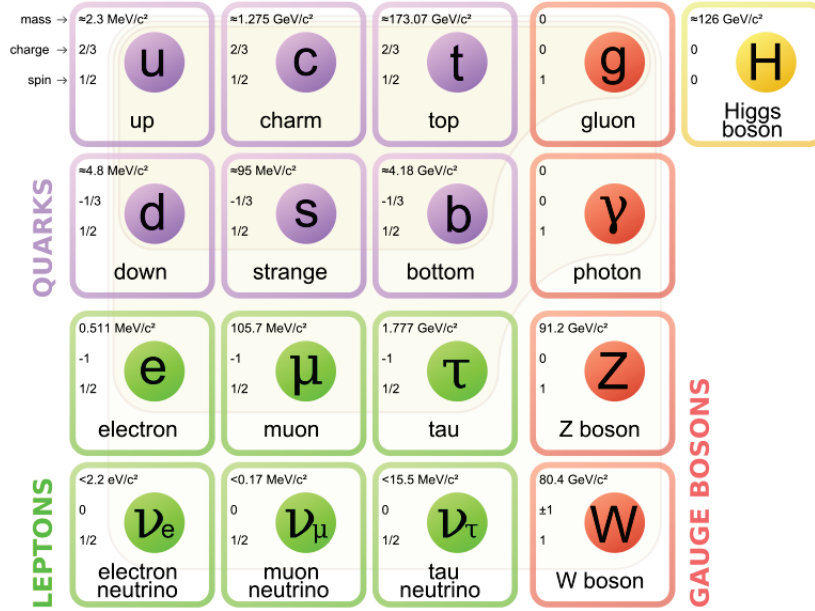


Figure 1: A pictorial representation of the Standard Model, including quarks, leptons and mediating bosons. Diagram adapted from [1].

boson. We are familiar with the electric charge of a proton, a measure of the strength with which the proton will interact with other particles via the electromagnetic interaction. Analogously, we may speak of the weak charge of the proton. This charge, denoted by Q_{weak}^p , describes the strength with which the proton interacts with other particles via the weak interaction. In the context of electron-proton scattering, the electron and proton interact weakly when they exchange a Z boson. Relative to the electromagnetic interaction, the weak interaction occurs with lower frequency because the electromagnetic force is much stronger than the weak nuclear force.

An important feature of many physical properties is their parity. A parity transformation indicates the inversion of all of the spatial coordinates of a system. When we speak of a parity inversion in terms of a particle interaction, it means that one is observing a mirrored copy of the original interaction. When parity is conserved, the mirrored interaction looks identical to the original copy. However, when parity is violated, then the mirrored copy of the interaction looks different from the original. Most fundamental interactions, such as those that occur via the electromagnetic and strong nuclear forces, are parity conserving. Interactions via the weak interaction, conversely, are parity violating; the Qweak experiment exploits this physical property in order to find the weak interactions among the stronger electromagnetic interactions.

The Qweak Experiment [2], run at Jefferson Lab, is a high precision test of the Standard Model via a measurement of Q_{weak}^p . In order to make a measurement of this quantity, we examine the elastic scattering of electrons off of a liquid hydrogen target. Because the weak charge is parity violating, there is an asymmetry between the scattering rate for right- and left-handed electrons. This asymmetry is calculated using the different scattering cross sections [3]:

$$A_{RL} = \frac{\sigma_R - \sigma_L}{\sigma_R + \sigma_L} \quad (1)$$

where σ_R is the scattering cross section for right-handed electrons and σ_L is the scattering cross section for left-handed electrons. The asymmetry is then used in the expression for the weak charge of the proton, Q_{weak}^p [3]:

$$A_{RL} = \frac{G_F}{4\pi\alpha\sqrt{2}} [Q_{weak}^p Q^2 + Q^4 B(Q^2)] \quad (2)$$

where Q^2 is the four-momentum transfer between the particles, G_F is the Fermi constant, α is the fine-structure constant that describes the strength of the electromagnetic interaction, and $B(Q^2)$ is a function of the momentum transfer and is determined by the internal structure of the proton. The expression yields the weak charge of the proton, which is then used to calculate the weak mixing angle, θ_W , a parameter predicted by the Standard Model, using the expression for the weak charge [4]:

$$Q_{weak}^p = 1 - 4 \sin^2 \theta_W \quad (3)$$

The main goal of the experiment is to calculate the weak mixing angle and to determine whether it is in agreement with the Standard Model. Any deviation from the predicted value would indicate that there is new physics to be explored. In addition, any measured value of the weak mixing angle places limits on new theories being developed to supplement or alter the Standard Model [5].

2 Experimental Setup

The tracking portion of the experiment is involved in determining the motion of the electrons as they move through the experimental apparatus and, then, calculating the kinematic parameters of the flight, such as the momentum transfer, scattering angle and scattered energy. The tracking runs

were collected with lower beam current so that the sensitive equipment used for measurements was not destroyed or overwhelmed, and so that the kinematics for individual events could be calculated. The production- or current-mode, for measuring the asymmetry, was run at a beam current of $180\mu\text{A}$; the tracking-mode, or event-mode, for tracking the electrons, was run at 200pA , about a million times smaller than current-mode.

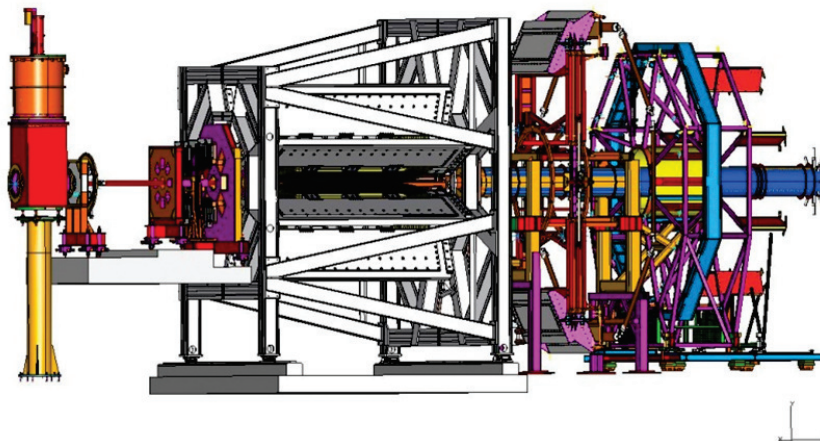


Figure 2: Experimental apparatus of the Qweak experiment. The beam travels from left to right through the LH2 target, HDCs, QTOR, VDCs, main detectors. Adapted from [6].

The beam of electrons comes into the experimental hall after being accelerated to energies of about 1.165 GeV and is incident on the liquid hydrogen (LH2) target; the experimental setup is shown in Figure 2. After an electron scatters, it leaves the target and passes through the horizontal drift chambers (HDCs), QTOR magnet, vertical drift chambers (VDCs) and finally reaches the main detectors on the far right.

2.1 Electron Beam and Proton Target

The electron beam is generated at the Continuous Electron Beam Accelerator Facility (CEBAF) at the Thomas Jefferson National Accelerator Facility in Newport News, Virginia. The electrons, when they are created, are polarized, meaning that the spins of the electrons are all pointed in one direction, ideally. The helicity of the electrons describes the direction in which the spin of the electron is pointing relative to the momentum of the electron. Right-handed electrons have the component of their spin pointing in the direction parallel to that of their momentum. Left-handed

electrons, conversely, have spin and momentum that are anti-parallel, as shown in Figure 2.1a. This distinction becomes important because the electron-proton scattering can happen in one of two ways. The electron and proton can interact via the electromagnetic interaction, by exchanging a photon, or they can interact via the weak force, by exchanging a Z boson. These possibilities are shown in Figure 2.1b. Both right- and left-handed electrons interact via the electromagnetic interaction with the same probability. However, because the weak interaction is parity-violating, right- and left-handed electrons interact with different probabilities. Thus, as mentioned in the previous section, an asymmetry in the scattering rate develops that can be measured and used to calculate the weak charge of the proton.

a)



b)

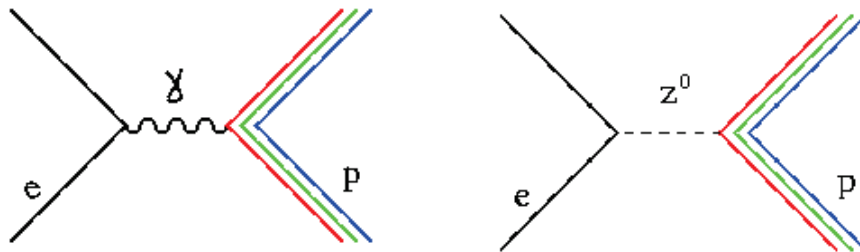


Figure 3: a) A pictorial representation of right- and left-handed electrons. b) The two possible scattering events, with the electromagnetic interaction (on the left) and with the weak interaction (on the right).

In order to eliminate any trends in the data due to environmental conditions or other factors, the helicity of the electrons is switched at 960 Hz. The flips are arranged in sets of four periods so that for two quarters the electrons will have positive helicity (right-handed) and for two quarters they will have negative helicity (left-handed). The arrangement of these positive and negative states is either positive-negative-negative-positive (+- -+) or negative-positive-positive-negative (-++-).

The starting helicity of each set of four is randomly chosen and the other three periods follow from this choice. This arrangement of the helicity is necessary in order to average out stochastic effects during analysis.

When the electron beam enters the experimental hall, it first encounters the liquid hydrogen target. The target is an aluminum shell that contains the hydrogen; it has thin aluminum windows on the front and back to minimize electron interactions with the aluminum. The target is liquid hydrogen because it is effectively a proton target, and because it has a high density, increasing the chances of an interaction between an electron and a proton. The target is wider at the back so that the scattered electrons have a lower probability of hitting the thick aluminum walls and scattering off of an aluminum atom as they leave the target. Some of the electrons in the beam do scatter off of the aluminum walls of the target; therefore, part of the experimental analysis is finding the contribution of the aluminum-scattered electrons and subtracting those events from the signal as a background, so that they do not skew the asymmetry results.

2.2 Drift Chambers

After the electrons scatter in the hydrogen target, they encounter the first set of drift chambers: the horizontal drift chambers. The other set, the vertical drift chambers, are located after the QTOR magnet, but they operate in the same manner as the HDCs. The drift chambers are boxes filled with a mixture of argon and ethane, containing many planes of wires and aluminum-coated Mylar foils [4]. As an electron moves through the chamber, it ionizes the gas. The wires are at ground (or at a small potential) while the foils are at a high voltage; therefore, when an electron ionizes the gas, the resulting electrons are repelled by the foils and attracted to the wires. This process induces a current, creating a signal in the wire. The current is measured and recorded, indicating when, where and in what direction the electron passed through the chamber. Because there are many wires in the chambers, a trajectory can be constructed for each electron that passes through them. The vertical drift chambers work in approximately the same manner as the HDCs, but are placed at an angle so that when the electrons are bent by the QTOR, they drift vertically through the chambers [4].

Because the horizontal drift chambers are very close to the target and are located before the QTOR magnet, many electrons pass through the drift chambers simultaneously. Consequently,

several of the wires in the drift chamber will have a signal at any moment in time. By using the timing of the electrons as they move toward the wires, one is able to determine the trajectory of the electron and, subsequently, its angle with respect to the plane of the wires. The vertical drift chambers have fewer electrons passing through them because the chambers are located after the QTOR magnet. The vast majority of the inelastic events are deflected by the magnetic field, and typically only one wire in the drift chamber has a signal at a given moment. In this case, it is not possible to use the drift times, as for the HDCs. Therefore, more planes of wires are needed to construct the trajectory of the electron through the chamber.

The HDC measurements are used to find the angle, θ , with which the electron scattered off of the proton. Measurements from the VDCs are used in conjunction with the HDC measurements and the QTOR current to reconstruct the track of the electrons and to determine the parameters associated with the flight. There are two vertical drift chambers and two horizontal drift chambers each; therefore, to obtain measurements in all of the octants, the chambers are mounted on a motorized arm that can be rotated so that each pair of octants can be studied in turn. The two chambers are called package 1 and package 2, respectively. The eight octants are arranged around the octagon, as shown in Figure 4. The octant pairs are: 1&5, 2&6, 3&7 and 4&8. The rotator for the vertical drift chambers was placed in such a way that it could have package 1 in octant 3 and package 2 in octant 7, or the position could be inverted so that package 2 was in octant 3 and package 1 was in octant 7. The rotator for the horizontal drift chambers could also produce a reversed run, but, in this case, it was octants 2&6 were the octants that were inverted. This position reversal is useful as a diagnostic to ensure that the packages were behaving identically. We expect to see the same results for the normal and reversed runs.

2.3 QTOR and Main Detectors

The electrons, next, pass through the QTOR (Qweak Toroidal) magnetic field. Because the electrons are charged, they feel a force due to the magnetic field and their trajectories bend when they pass through the field, as is shown in Figure 5. The amount by which the trajectory is altered is proportional to the strength of the magnetic field and inversely proportional to the momentum of the electrons. In addition to providing information about the energy of the elastically scattered electrons, the magnetic field also deflects unwanted, low-energy electrons, such as Møller-scattered

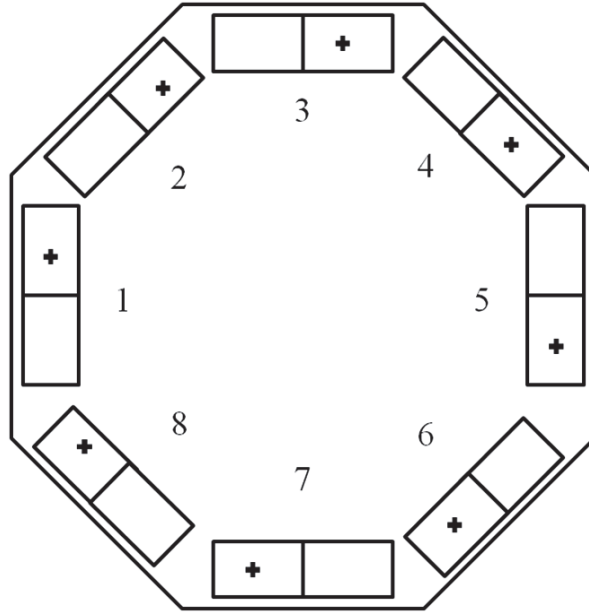


Figure 4: This diagram shows the arrangement of the eight octants. The + symbols indicate the positive end of each of the detectors.

electrons and inelastically-scattered electrons, as shown in the top picture in Figure 6, by bending the trajectories so that very few of those electrons pass through the next set of drift chambers [5]. Elastically-scattered electrons, however, have higher energy and are able to pass through the magnetic field with a smaller bend to their trajectory. Through the use of the magnetic field and several sets of collimators, most of the electrons that make it to the vertical drift chambers and the main detectors are the elastically-scattered electrons.

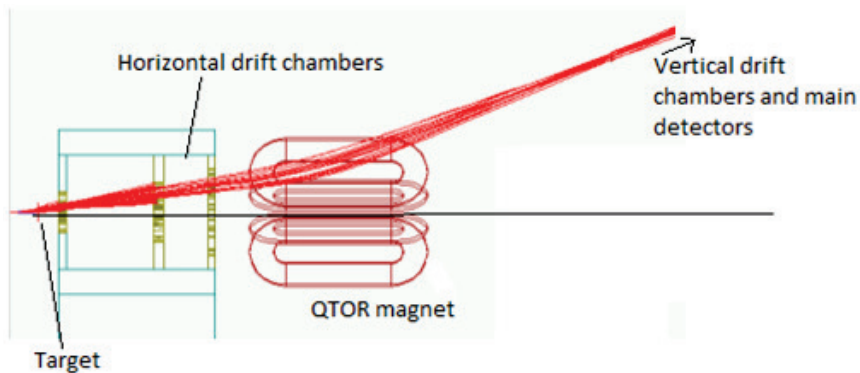


Figure 5: The paths of the electrons are bent as they pass through the QTOR magnet based on the energies of the particles and the strength of the magnetic field. Adapted from [7].

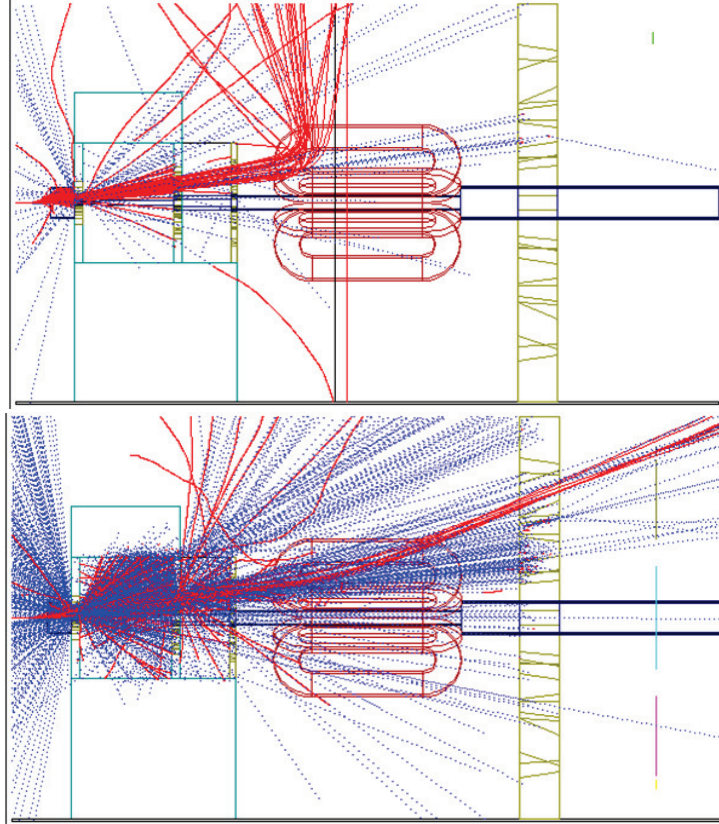


Figure 6: These diagrams show the effect of the magnetic field on the scattered electrons. Möller-scattered electrons are largely deflected by the magnetic field. Elastically-scattered electrons (bottom figure) are also deflected, but with a smaller magnitude. Figures adapted from [4].

Finally, immediately behind the VDCs are the main detectors. They are made of a synthetic quartz that emits photons when electrons strikes them [7]. A full detector bar is made of two 1 meter bars that are glued together. The glue joint in the center causes some light attenuation in the detector; however, although this is a defect, the location of the glue joint has proved to be a useful diagnostic tool for verifying the relative positions of the main detectors and vertical drift chambers, in order to check the geometry of the system.

Located immediately before the main detector bars is a thin lead preradiator. When the scattered electrons hit the lead, ionization occurs and a shower of electrons is produced. This electron shower continues on to the quartz detector where they produce Cerenkov radiation. Cerenkov radiation is produced because the electrons, although moving slower than the speed of light in air, are moving faster than the speed of light in the quartz. Therefore, the electron excites the atoms in the quartz, which then return to their original state by emitting a photon. A single electron in

the main detector can generate a cascade of photons. These photons bounce around inside of the detector until they hit a photomultiplier tube (PMT). The PMT sees the light as an indication that an electron made it to the detector and records the event as a hit. In addition, the detectors are positioned such that only the elastic events, when they are bent by the magnetic field, enter and are detected.

3 Track Reconstruction

In addition to the experimental data gathered at Jefferson Lab, we run Monte Carlo simulations of the experiment under different conditions. We make corrections to the simulations, such as modifying the coded geometry, and to the experimental data, by disregarding data that may be noisy or erroneous. The purpose of the simulations is to closely match their results to the results obtained from the experimental data. The simulated target, QTOR and detectors are implemented in GEANT4, the software used to run the simulations. The program then throws, typically, 125,000 random events at the target and, based on the parameters given to the simulation, the electrons' kinematic parameters are recorded and saved into a ROOT file.

In both the case of the experimental data and of the simulation, specific values such as the signals from the drift chambers and the hits in the main detector are recorded, as this is what can physically be measured in the experiment. To make this information useful for analysis, the actual tracks of the electrons need to be reconstructed. The signals from the HDCs and VDCs are recorded as hits on the wires to which the electron passes the closest. This can, in turn, be viewed as a trajectory through the chamber, and is characterized by a slope. As the electron flies through the QTOR, its trajectory is bent, as mentioned previously, by an amount that is proportional to the current in the QTOR and inversely proportional to the momentum of the electron. Therefore, using the recorded current, one can determine the energy of the electrons [4, 5]. In addition, the bent trajectory through the magnetic field is used to link up the tracks through the drift chambers. When a path matches the slopes in the drift chambers and the path through the QTOR to the correct tolerance, it is recorded as the track of the electron.

These tracks are projected back to the scattering vertex in the target, and forward to the main detector, so that there is a track for the electron for the entire length of the apparatus. In addition

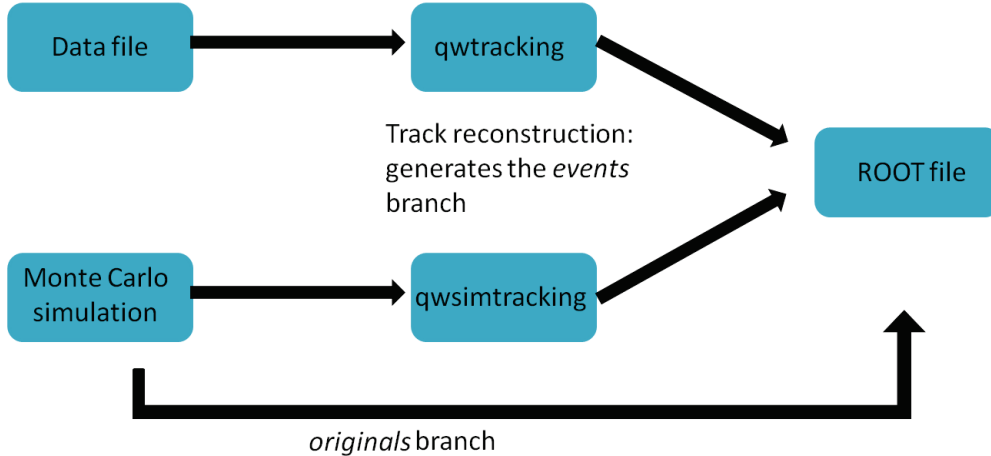


Figure 7: A simplified visual representation of the track reconstruction process. The output ROOT files have either only an *events* branch, in the case of a data file, or both *events* and *originals* branches, in the case of a simulation file.

to determining the scattered energy, E' , of the scattered electrons from these reconstructed tracks, we can also use the track information to test other parts of the experiment. We can restrict the data to include only a specific location of the scattering vertex in the target, in order to look at electrons that scattered in the very center of the target. We can also examine the distribution of hits in the main detectors, and use the information to determine the edges of the detectors to compare with the survey data of the apparatus to ensure that they match.

All of these reconstruction calculations are completed using an analyzer called *qwsimtracking* for simulated files, and *qwtracking* for data files. A flow chart of this process is found in Figure 7. After the simulation ROOT file is run through the analyzer, the output ROOT file contains two branches: *events* and *originals*. The *originals* branch contains all of the events that are thrown at the target during the simulation. It also includes all of the scattering angles, momenta and other kinematic parameters without any reconstruction. The second branch is *events*, which contains only the reconstructed events. The *qwsimtracking* analyzer creates this branch, which includes the reconstructed momenta, energy and scattering angles based on the measurements that the simulation made in the horizontal and vertical drift chambers, the QTOR current, the beam energy and any other parameters that were specified in the simulation. The tracking analyzer also converts the individual tracks of the simulation to the main detector hits in the experimental data files.

The experimental data ROOT files only have an *events* branch because it was only possible

to measure certain values in the experiment. The remaining parameters of the trajectories of the electrons have to be calculated from these values. Therefore, there was no original branch and no non-reconstructed variables. Once the simulation ROOT files and the experimental data files were of the same type and contained the same branches and variables, I was able to begin analyzing the kinematic parameters, such as momentum transfer, Q^2 ; scattering angle, θ ; and scattered energy, E' .

4 Momentum Transfer: Q^2

The main purpose of the tracking portion of the Qweak experiment is to determine a value for the four-momentum transfer, Q^2 , between the electron and the proton. Qweak examines the scattering events that have a small momentum transfer, or a low Q^2 . This means that the electrons are not hitting the protons very hard, just ‘tickling’ them. As mentioned in the introduction, there is an equation (equation 2) for the asymmetry that depends on Q^2 . Because Q^2 appears in the asymmetry equation in several places, the uncertainty on the value of Q^2 must be very small so that the uncertainty on the final value of Q_{weak}^p remains within the acceptable limits for the experiment. There are several equations used to calculate Q^2 , depending on a combination of the initial energy of the electron, scattered energy of the electron and the scattering angle of the electron. All of the equations assume that the electrons were elastically scattered. In addition, they are all equivalent to each other, mathematically, but because some of the variables have a higher precision than others in the experiment, it is necessary to use the equation that gives the most precise value of Q^2 .

The most general Q^2 equation is:

$$Q^2 = 4EE' \sin^2 \theta / 2 \tag{4}$$

where E is the initial energy of the electron, E' is the scattered energy and θ is the scattering angle. It uses all of the kinematic parameters at our disposal. The next equation depends only on E and θ :

$$Q^2 = 2E^2 \frac{1 - \cos \theta}{1 + \frac{E}{M}(1 - \cos \theta)} \tag{5}$$

It has the advantage of being independent of E' , which depends both on the scattering angle and

the track reconstruction through the vertical drift chambers, making it the least precise of the three variables. The third Q^2 depends only on E' and θ :

$$Q^2 = 2E'^2 \frac{1 - \cos \theta}{1 - \frac{E'}{M}(1 - \cos \theta)} \quad (6)$$

This equation is independent of E , the initial energy of the electron. E is determined from the energy of the beam and is the most precisely known of all of the variables present in the Q^2 equations. The final Q^2 equation depends only on E' and E :

$$Q^2 = 2M(E - E') \quad (7)$$

This equation is independent of the scattering angle, θ , which is determined from the data from the horizontal drift chambers and survey data of the experimental apparatus. In all of these equations, M is the mass of the proton; the mass of the electron is neglected in the experiment because it is small compared to the mass of the proton. Because E' is the most imprecise of all of the variables, we choose to use equation 5 to calculate the most precise value of Q^2 .

The determination of Q^2 is the part of the experiment in which the Monte Carlo simulations become very important. In a previous section, I mentioned that it is necessary to make corrections to the simulation so that the distributions we obtain from simulation match very closely the distributions that come from the data collected during the course of the experiment. This is because the value of Q^2 that is used in the calculation of Q_{weak}^p is the value that is obtained from simulation. The reason for this is simple, there are so many unknowns associated with the actual experiment that it is not feasible to attempt to calculate Q^2 from the data collected.

For example, the energy of the electron beam before it reaches the hall is fairly well documented; however, as soon as the electrons enter the hydrogen target, they begin to lose energy. This means that the initial energy, E , of any scattering event is unknown because the amount of energy loss will be affected by the location in the target at which the electron scattered. Then, after the scattering event, the electron will continue to lose energy as it passes out of the remainder of the target and into the air of the hall. The electrons also lose energy when passing through the drift chambers. Therefore, when the electron track is reconstructed using the measurements from the

drift chambers, we obtain a scattered energy, “ E' .” This is only an approximation of the actual energy of the electron immediately after it scatters off of the proton in the target. Then, using equation 4, we are able to calculate “ Q^2 .” Again, this can only be an approximation because we are unable to account for all of the energy losses that the electron experiences as it travels through the experimental apparatus.

Consequently, because we are unable to accurately calculate the scattered energy or momentum transfer from the experimental data, we, instead, use the value that comes from the simulation. We make corrections to the simulation, such as changing the geometry so that it exactly matches the geometry from the physical experiment, until the simulation matches the results from data to the desired precision. Then, the value of Q^2 and its uncertainty will be extracted from the simulation and used in subsequent calculations of Q_{weak}^p . There must be very good agreement between data and simulation because the value of Q^2 needs to be very precise. The budgeted uncertainty for Q^2 within the experiment is 0.5% [5]. The low uncertainty is necessary because, as mentioned in the introduction, the Qweak Experiment is a high precision test of the Standard Model. The final result for Q_{weak}^p must have an uncertainty less than 4% [4], meaning that each of the component values used to calculate the weak charge must remain within their budgeted uncertainty.

5 Analysis

The main goal of my project was to verify that the kinematic parameters match between simulation and data. The three parameters that I focused on are the momentum transfer, Q^2 ; the scattering angle, θ ; and the scattered energy, E' . Each simulation file, as I mentioned before, is divided into two sections: *events* and *originals*. The *originals* section contains the information from all of the events thrown during the course of the simulation, before any track reconstruction has been done. The *events* section is generated by the *qsimtracking* program, and contains only information about tracks that have been reconstructed. The kinematic parameters that I studied, with the exception of E' , were stored in both sections of the simulation file. I used ROOT to generate histograms of the variables, while applying different cuts, or allowable restrictions, to the data. I used data files stored on tape at Jefferson Lab, and I remotely copied certain files from the tape storage as I needed them. I also copied the simulation ROOT files; the simulations that I have been using

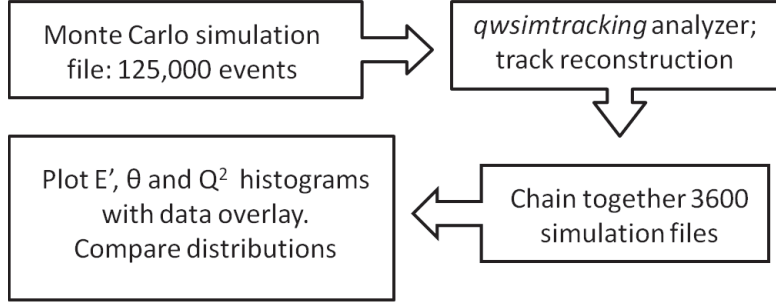


Figure 8: A simplified visual representation of my analysis process, beginning with the raw Monte Carlo simulation files. After track reconstruction analysis, I use the files to generate many types of histograms.

are light-weighting scans (weighting the output of the main detector with the number of photons produced by the detector in different locations [5]) generated by Valerie Gray, one of the graduate students associated with the experiment.

I ran 3600 of the simulation files through the *qwsimtracking* analyzer to obtain the variables needed for my work. In each of my scripts, I linked all of the simulation ROOT files together, creating a set of simulated data that included the events contained in all of the constituent files. A flow chart for this analysis process is shown in Figure 8. To begin, I plotted different combinations of the histograms (simulation *events*, simulation *originals* and data *events*) of Q^2 . In addition, all of the histograms from the simulation are weighted with the scattering cross section distribution. The Q^2 script generated three plots: simulation originals and simulation events; simulation events and data, and simulation originals and data. The set of three Q^2 plots is found in Figure 9. I had a similar script for the scattering angle, θ ; it generated the same three plots. The θ plots are in Figure 10. The final script was for E' ; the *originals* section of the simulation file does not contain an E' leaf, as the scattered energy is only a reconstructed value. Therefore, I could only plot one histogram, simulation events and data, found in Figure 11.

The Q^2 and θ plots seem to show that the simulation constructs electron tracks with the proper momentum transfer and scattering angle. There were some discrepancies, but nothing that appeared to be out the ordinary or that could not be fixed without some fine-tuning in the simulation, or calibration and analysis. The most interesting result is seen in the E' , because the mean scattered energy from simulation is higher than the mean scattered energy measured in the

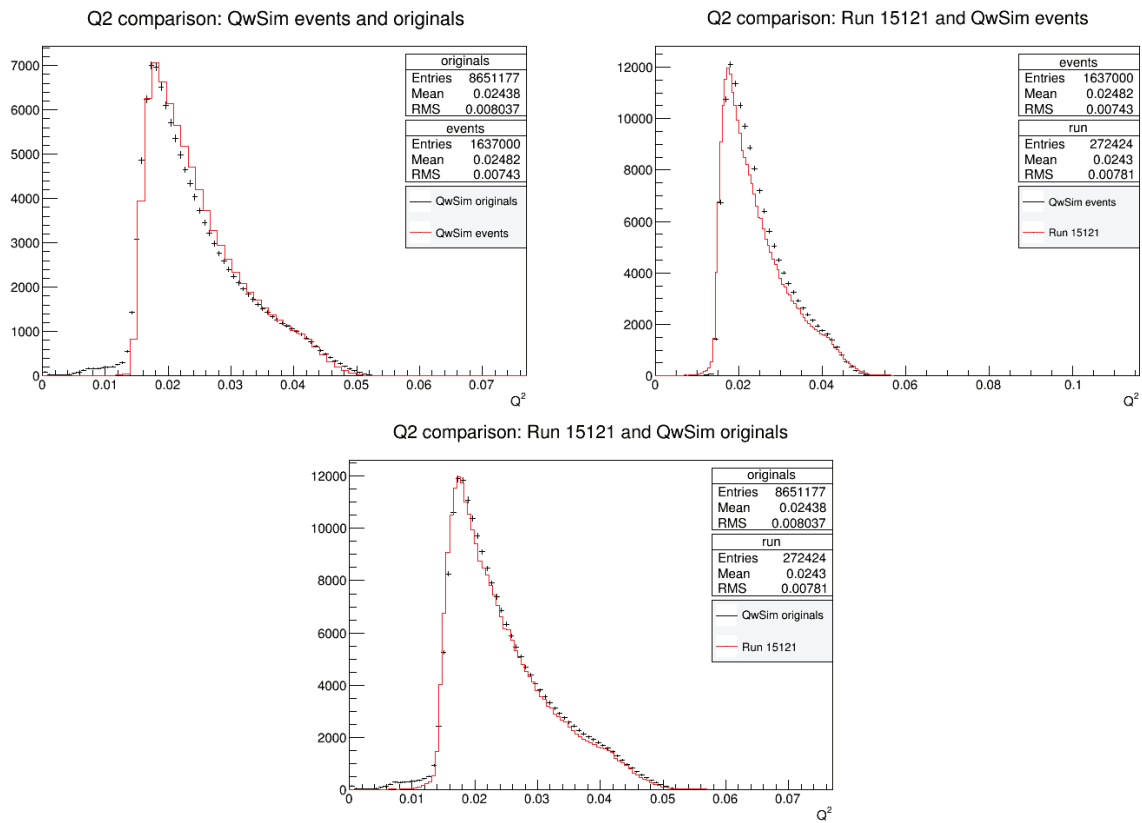


Figure 9: The Q^2 comparison plots using data run 15121.

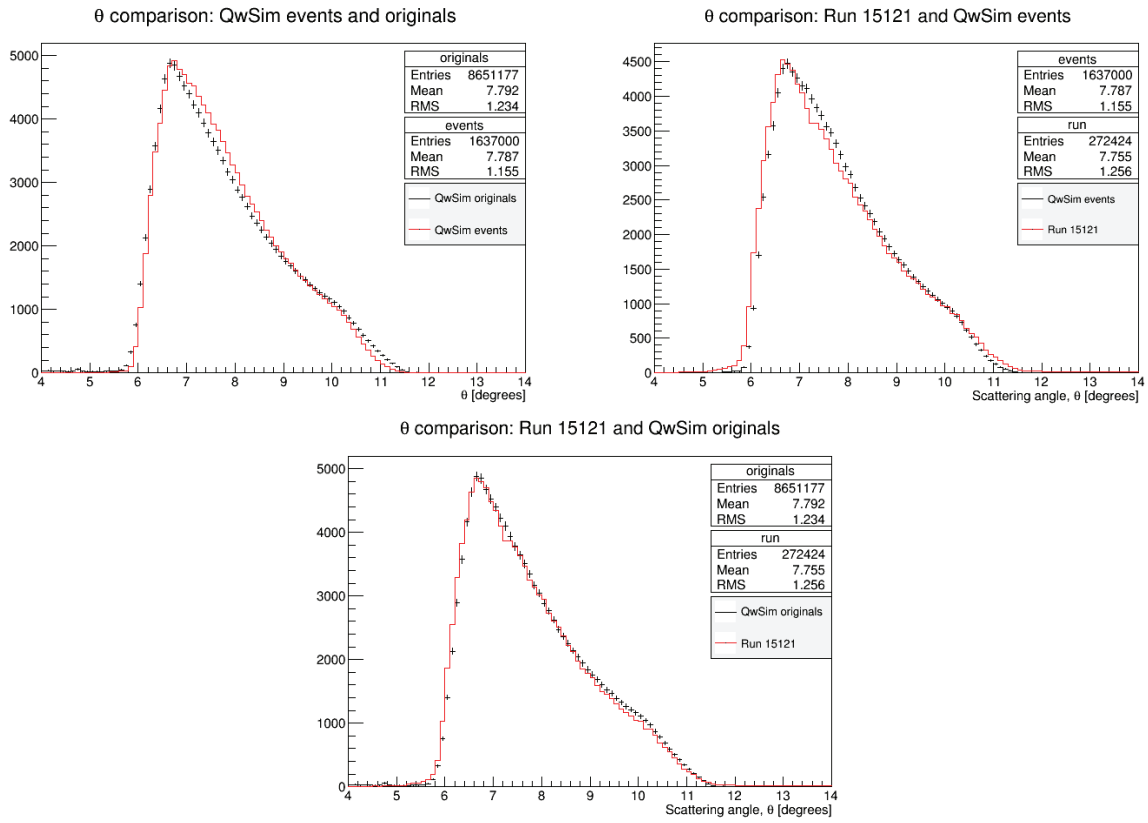


Figure 10: The θ comparison plots using data run 15121.

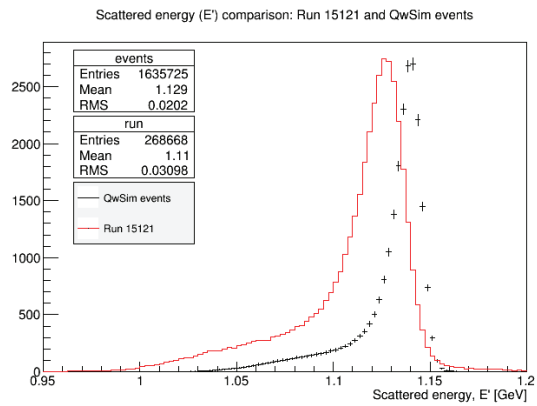


Figure 11: The E' comparison plot using data run 15121.

experiment. We thought, for a time, that the simulation might not be implementing energy loss processes, such as bremsstrahlung radiation and multiple scattering, properly. I ran some new simulations with different energy loss processes inactivated to examine the effect on the scattered energy distribution. I started with a simulation that had none of the energy loss processes activated. Then, for each subsequent simulation, I reactivated one energy loss process in the following order: Cerenkov radiation, photons, ionization, Compton scattering, bremsstrahlung radiation and multiple scattering.

Energy loss process study: E' means	
Processes activated	E' mean (GeV)
None	1.152
Cerenkov	1.152
Cerenkov, photons	1.152
Cerenkov, photons, ionization	1.136
Cerenkov, photons, ionization, Compton	1.136
Cerenkov, photons, ionization, Compton, bremsstrahlung	1.127
Cerenkov, photons, ionization, Compton, bremsstrahlung, multiple scattering	1.128

Table 1: Table of the activated energy loss processes and the mean value of E' from each simulation. We can see the effect of each process on E' based on the relative shift of the mean scattered energy.

I plotted the E' distribution from data, E' from the unmodified simulation and E' from the modified simulation. When I generated the histograms, shown in Figure 12, the mean scattered energy did move depending on the processes that were activated. Table 1 is a compilation of the mean E' values for each of the simulations. We can see that there is a larger change in the mean E' when bremsstrahlung radiation and ionization are added back to the simulation, and smaller changes associated with the other energy loss processes. However, there was no behavior that was unexpected or that would explain the drastic differences between the scattered energy in data and simulation.

Next, we decided to add some cuts to the data, in order to determine whether there was an energy bias for electrons with a certain scattering angle or scattering vertex location. I modified my script to take only those events with a scattering angle of $6.5^\circ < \theta < 7.5^\circ$ and a scattering vertex in the center of the target to remove effects of the electrons interacting with the aluminum

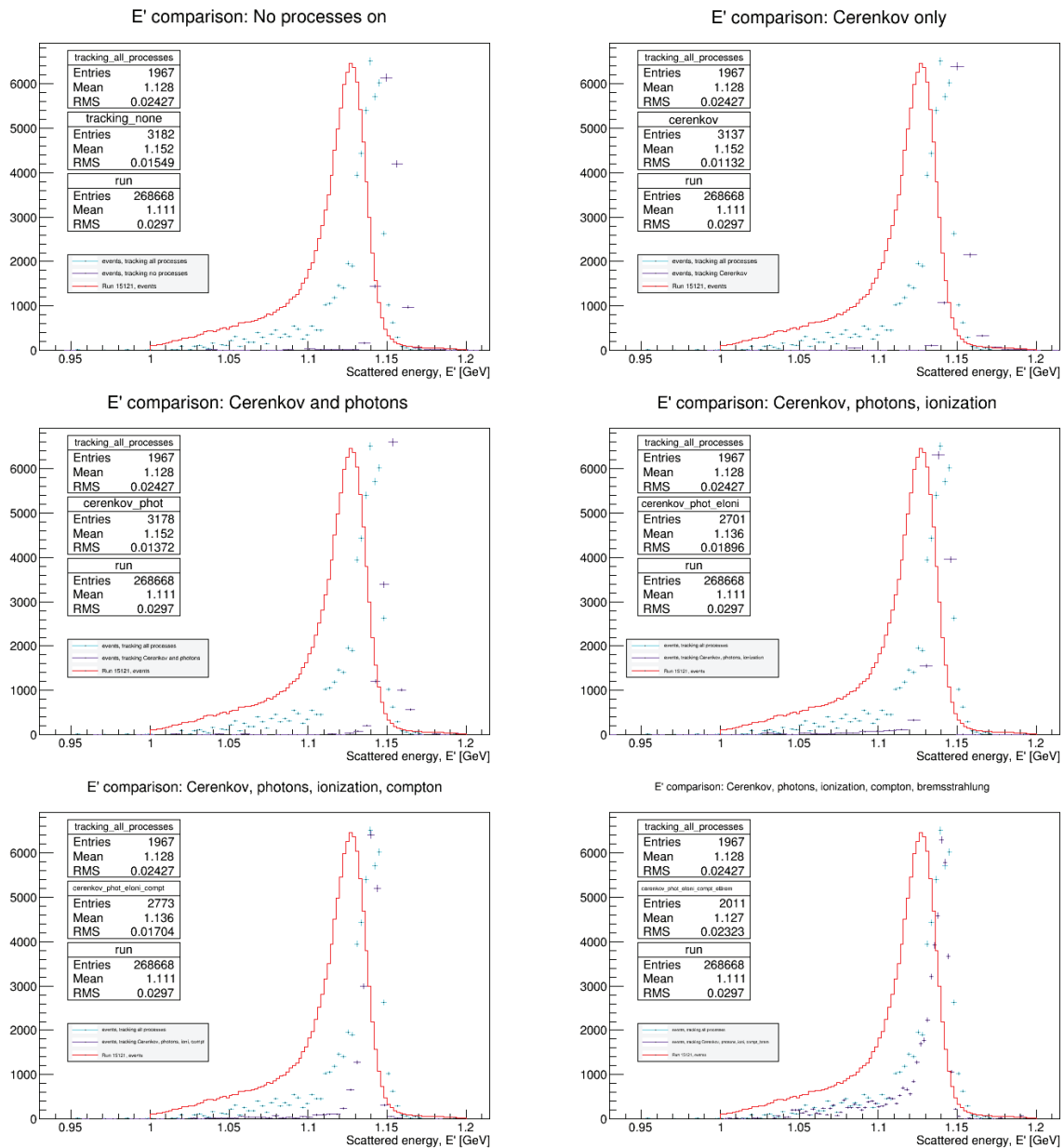


Figure 12: These plots show the six different simulations that I ran. Beginning with no energy loss processes activated, and then adding back in, respectively, Cerenkov, photons, ionization, Compton scattering, bremsstrahlung radiation and multiple scattering. Modified simulation (purple), unmodified simulation (blue) and data file (red) are plotted.

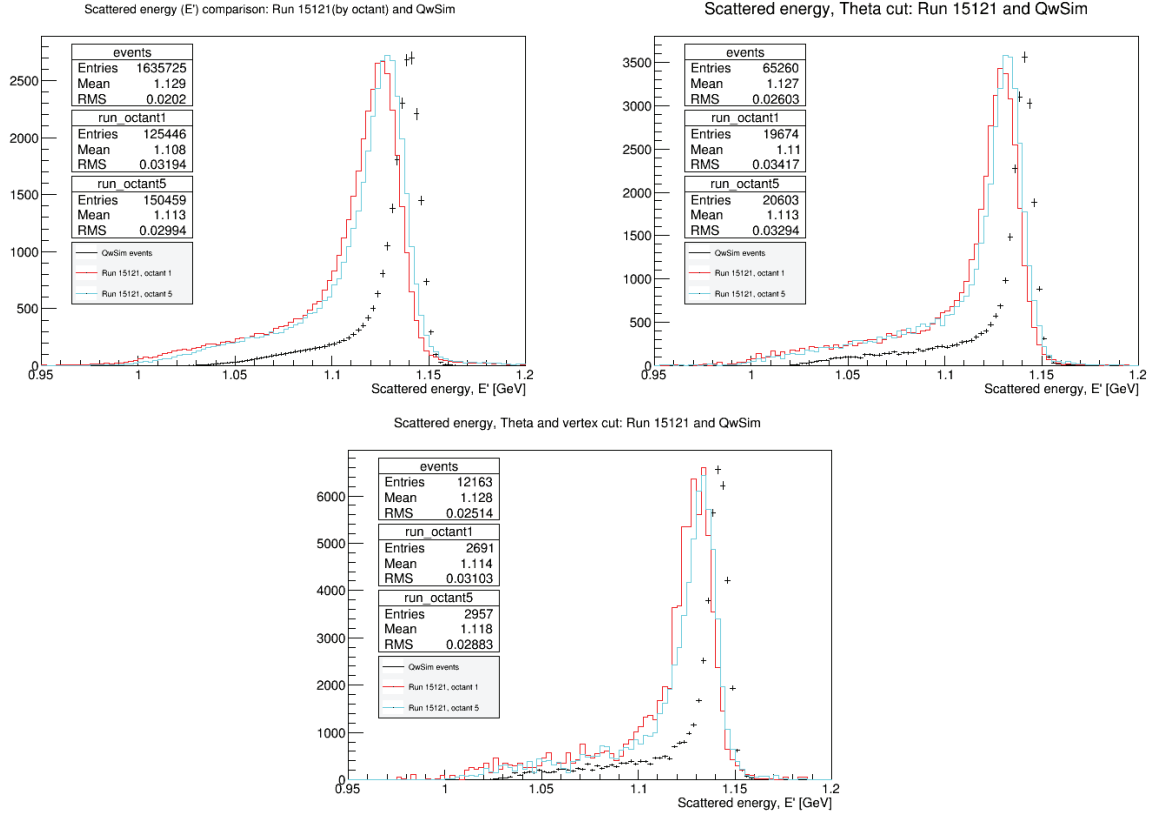


Figure 13: The E' comparison plots with cuts on package, scattering angle and vertex location, using data run 15121. Simulation (black points) and data (red and blue lines) are shown in these plots.

walls of the target. In addition, I added a cut that split the experimental data into two packages, one for each drift chamber, in case there was some anomaly that was causing the mean scattered energy from both octants to be lower than it should be. Recall that there were only two horizontal and two vertical drift chambers, located in the octants directly across from each other. Therefore, I split the histograms so that each octant was plotted separately. Although the cuts did make the mean scattered energy from experiment and simulation closer together, there was still a large discrepancy, as shown in Figure 13.

Next, I plotted the same histogram for E' , but using data runs other than run 15121, in case this anomaly was run-specific. I pulled several data files, many of which had the drift chambers in different octants to run 15121. I ran my scripts with the new data files and found something unexpected. Although the shape of the E' distribution is still incorrect, in some of the octants the mean scattered energy occasionally matches between simulation and experiment. This is shown in

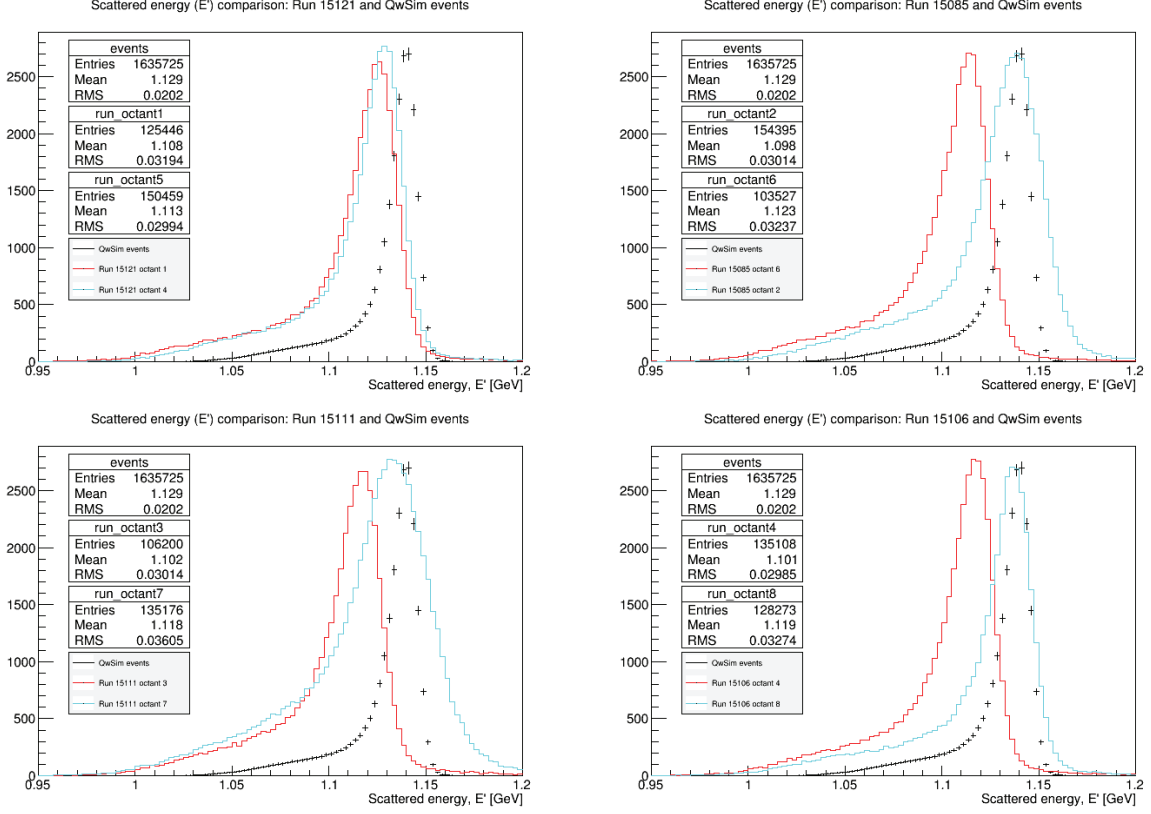


Figure 14: The E' comparison plots with different experimental data files. Note the approximate scattered energy mean matches in octant 6 (run 15085) and octant 8 (run 15106).

Figure 14 in the top right and bottom right plots. I ran the scripts for these plots, with files with data from all of the octants for three of the running periods and obtained similar results to those shown in the Figure 14, with matches in octants 6 and 8.

The next diagnostic tool we used was to calculate the E' distribution that would be expected from the scattering angle distribution that is determined from the horizontal drift chambers. I took two of the equations used to calculate Q^2 (equations 8 and 9) and combined them to eliminate the dependence on Q^2 .

$$Q^2 = 2EE'(1 - \cos \theta) \quad (8)$$

$$Q^2 = 2E^2 \frac{1 - \cos \theta}{1 + \frac{E}{M}(1 - \cos \theta)} \quad (9)$$

$$E' = \frac{E}{1 + \frac{E}{M}(1 - \cos \theta)} \quad (10)$$

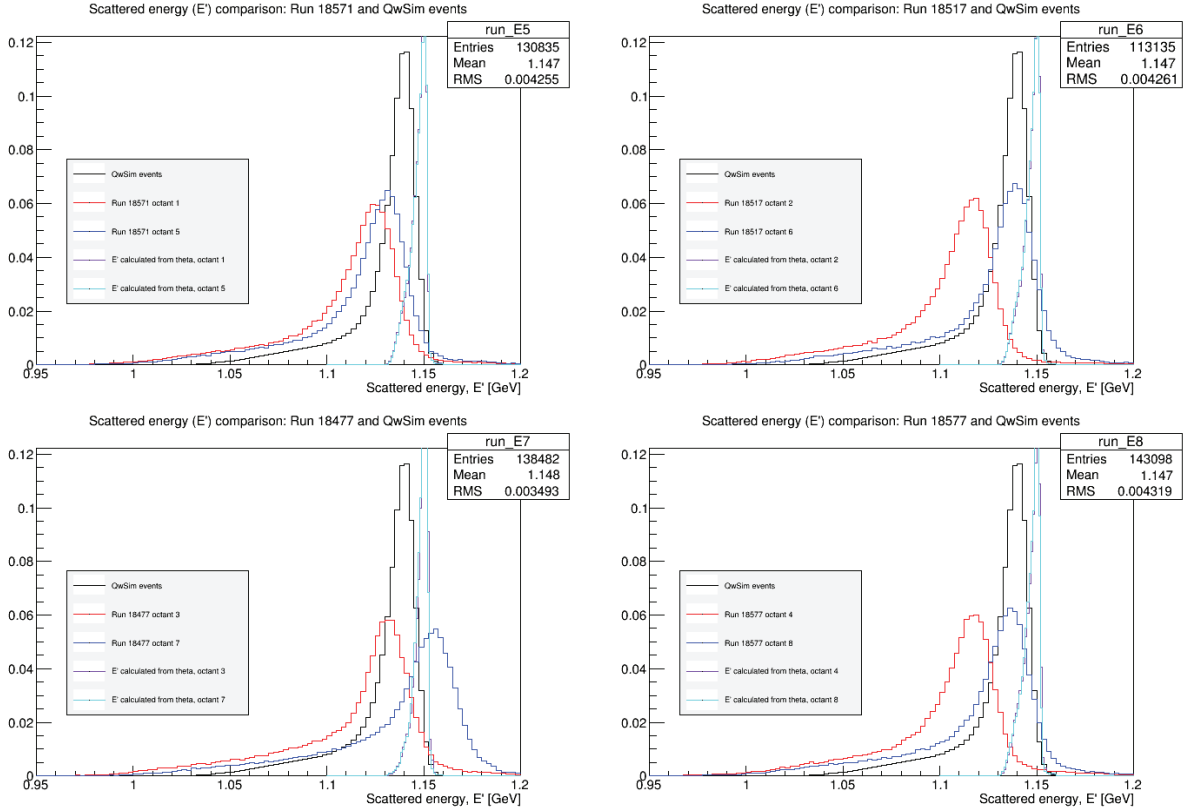


Figure 15: E' comparison plots covering all 8 octants. These plots show E' from data and simulation normalized to each other (red and dark blue), the calculated E' distribution from the θ distribution (purple and light blue) and E' from simulation (black).

Then, I was able to solve for E' , in terms of E , the initial energy of the electron; M , the mass of the proton; and θ , the scattering angle of the electrons, as shown in equation 10. The formula for the E' calculation is only valid for elastically scattered electrons. The behavior of any inelastic events or Møller electrons and their scattered energy is not described by the equation. I calculated E' with the corresponding θ distribution for each of my runs, again covering all eight octants. I, then, plotted the calculated distribution along with the E' from data and from simulation, as before. These distributions are shown in Figure 15. Because the scaling method I had been using was inefficient and imprecise, I used a different command to plot these histograms. With the new method, the histograms are normalized to the cumulative number of events. When I ran the plots again, the shapes of the histograms were approximately the same as before.

The notable features of these graphs are the positioning and shape of the calculated E' distribution with respect to the E' from data and with respect to each other. It is expected that

the calculated distribution will have a sharper peak and will have a larger mean E' because it is calculated from the energy of the electrons before they passed through the QTOR magnetic field. Thus, the electrons will not have experienced the energy losses associated with the bending of their trajectories when they travel through the magnetic field. This is exactly the effect that we see in the plots, with the sharp, calculated peaks located at higher E' than the E' reconstructed from data.

The other important feature from these plots is the location of the peaks with respect to each other. There are two peaks, corresponding to the two packages of the vertical drift chambers. In all four of the plots, we see that the calculated E' peaks are right on top of each other, indicating that the horizontal drift chambers expect that the E' distribution will be the same for all octants. This is not in agreement with the E' reconstructed from data, with measurements from the horizontal and vertical drift chambers. Because an octant dependence appears for E' from data, this would indicate that the effect comes from the vertical drift chambers, as this is the only major change between the calculated E' and the reconstructed E' .

In all of my plots, I obtained a mean value for the scattered energy. I shared this information with Dr. David Armstrong, who also works on the tracking portion of the Qweak experiment. Independent of me, he examined the octant dependence of E' . In particular, he took the actual location of the main detectors and the projected location of the main detectors from the vertical drift chambers, and found the difference between these locations. Because of the geometry of the system and the efficiency of the main detectors, this radial difference is approximately -1 cm. He, then, plotted the radial difference versus octant, as shown in Figure 16. In the figure, we see that there is a clear sinusoidal trend to the data. This means that, for some octants, the difference between the projected and nominal position of the detectors varies from the expected -1 cm difference, indicating a possible discrepancy in the geometry of the system. For example, if the geometry were aligned properly, then we would expect Figure 16 to be a horizontal line at -1 cm.

In the experiment, as mentioned previously, when an electron enters the main detector, a shower of photons is generated. These photons are detected by the photomultiplier tubes (PMTs) located on the ends of the quartz bars. In order for a hit to be recorded in the main detector, the time-to-digital converters (TDCs) connected to the PMTs on the detector must both fire within a certain time window. This means that if one TDC were to fire, then the other must fire within a specified

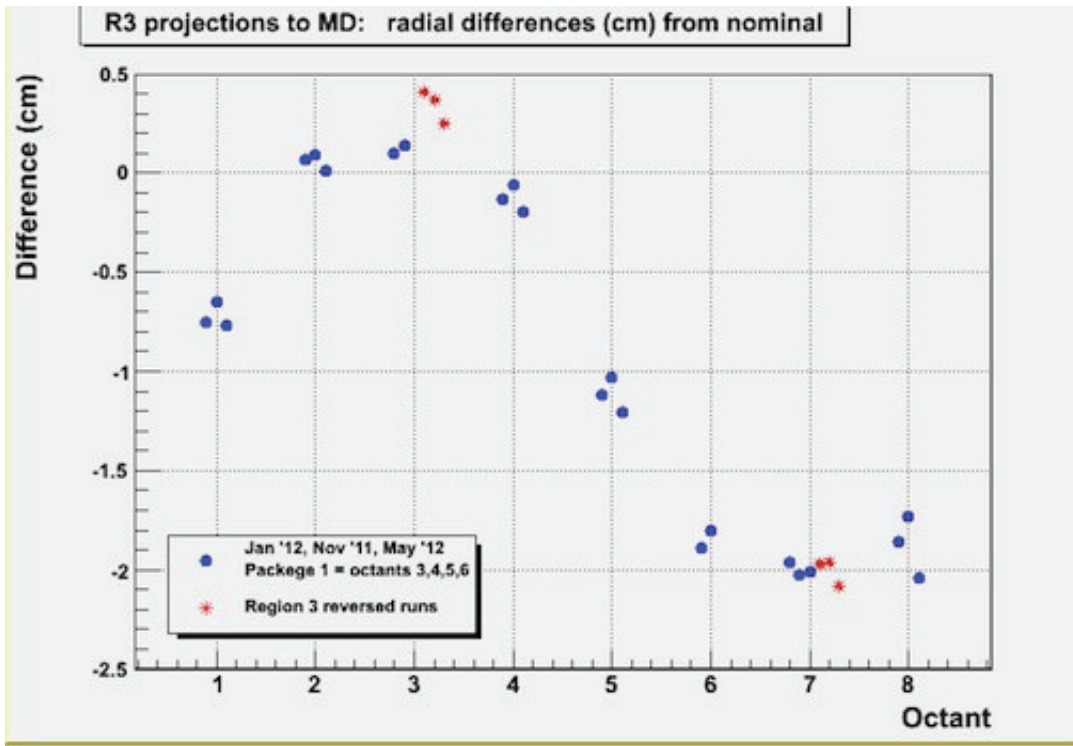


Figure 16: This is a plot of the difference between the actual location of the main detectors and their projected position from Region 3. There is a clear sinusoidal dependence, which is consistent with the rotator, on which the drift chambers are mounted, being slightly tilted. Plot generated by David Armstrong and adapted from [9].

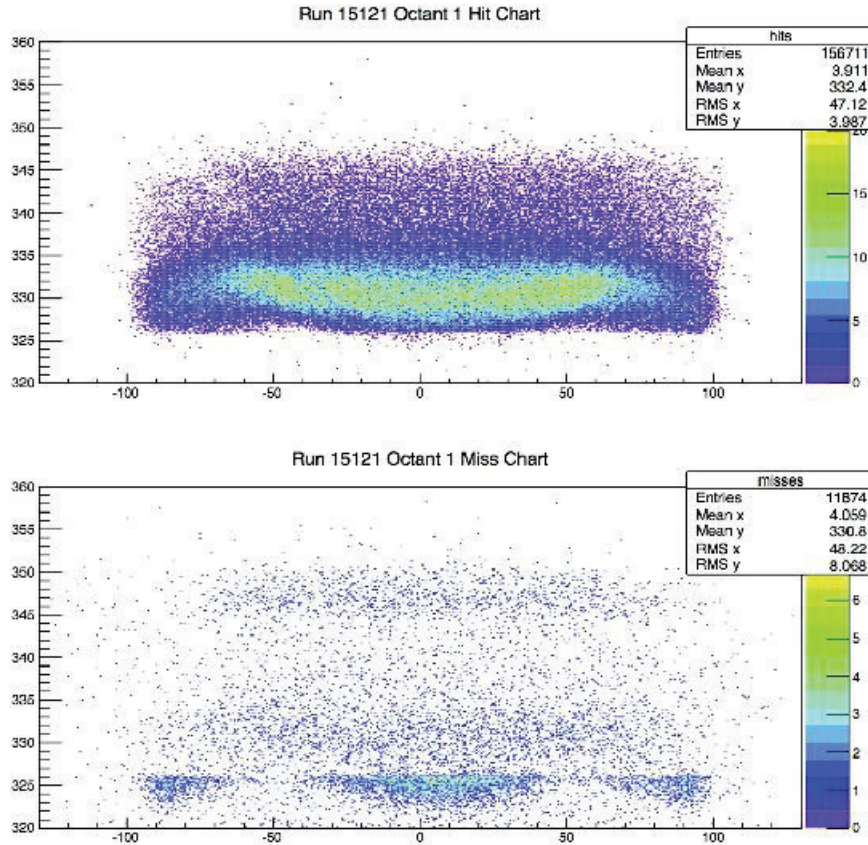


Figure 17: Distributions of hits (top) and misses (bottom) in the main detector in octant 1 for run 15121. Hits are characterized by the TDCs attached to either end of the main detector firing within -150ns to 200ns of each other. Note the characteristic “mustache” shape of the main detector hit distribution. Plot generated by David Armstrong and adapted from [10].

time for the electron track to have been considered a hit. If the TDCs do not fire together then the track is considered a miss. We can plot the distribution of hits and misses in the main detector, as shown in Figure 17.

Given the distribution of hits and misses of electron tracks in the main detector, one may determine the efficiency of the detector. First, it is necessary to calculate the number of hits divided by the sum of hits and misses. Then, this value is plotted versus the radial location in the detector, yielding a distribution of the efficiency of the detector, as shown in Figure 18. The efficiency increases sharply, indicating the inner edge of the detector bar, and then reaches a plateau where the efficiency is approximately constant. Then the efficiency drops off again, more gradually this time, showing the outer edge of the detector. We can use this efficiency plot to determine the

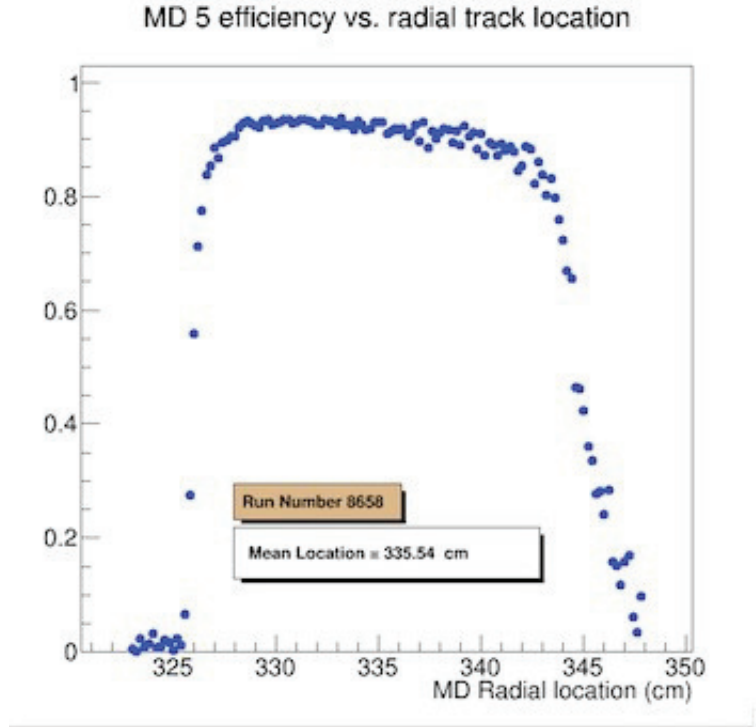


Figure 18: This figure shows the efficiency of the detector in octant 1 for run 15121. The sharp edge on the left hand side of the plot (at smaller radial position) indicates the inner edge of the detector bar. Plot generated by David Armstrong and adapted from [10].

radial location of the inner edge of the main detector. Furthermore, because this radial location should be constant for all of the octants, we can use any discrepancies to troubleshoot possible issues with the geometry of the system.

Using the mean E' values that I had compiled from my plots, Dr. Armstrong plotted the E' value versus the radial position differences, shown in Figure 19. In this graph we see a linear relation between E' and the difference between the nominal and projected locations of the main detectors. As I mentioned before, we expect the radial difference to be -1 cm. Octants 2, 3 and 4, at the top of the ring of detectors, all project the main detector higher than we expect, such that the radial difference is closer to 0 cm. This higher projection corresponds to a smaller scattered energy E' . Octants 6, 7, and 8, at the bottom of the ring of detectors, all project the main detectors lower than we expect, such that the radial difference is closer to -2 cm. The lower projection of the main detector now corresponds to a higher scattered energy. See Figure 4 for the arrangement of the octants. The linear relationship that we see between E' and the location of the octants on the ring

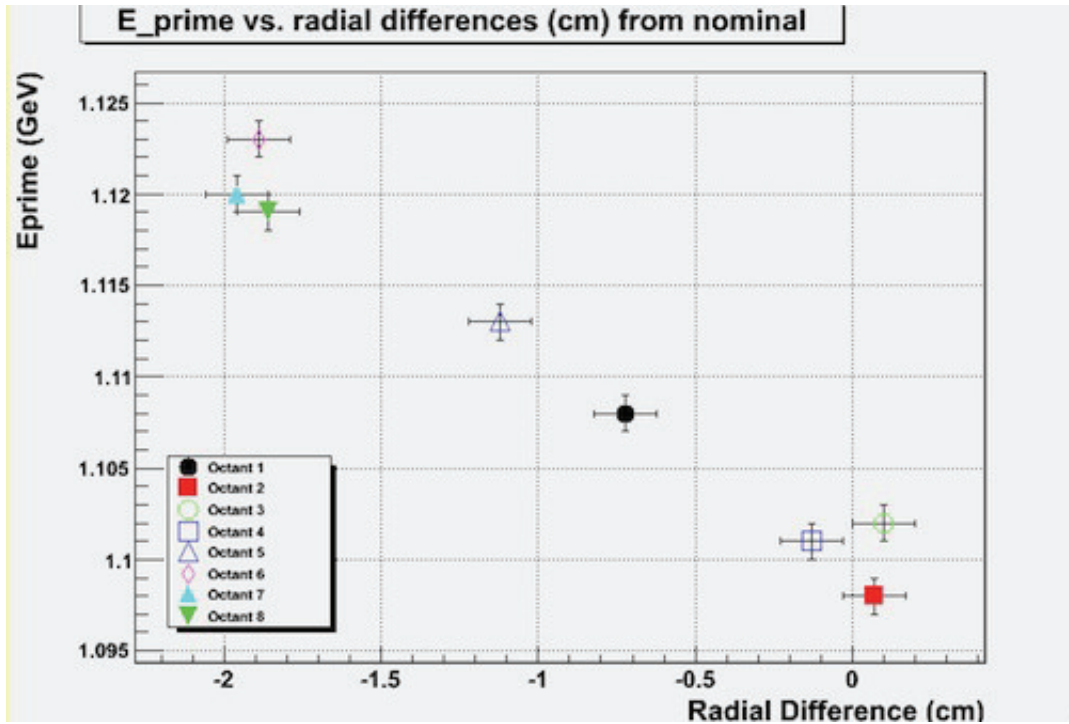


Figure 19: This plot shows the mean E' values that I found versus the radial difference between the nominal position of the detector and the projected location. The linear trend seen here is consistent with a tilt in the rotator holding the vertical drift chambers. Plot generated by David Armstrong and adapted from [9].

is consistent with the rotator being tilted slightly backward from the vertical.

With the new hypothesis that the rotator holding the vertical drift chambers was tilted on its axis, I have been working on characterizing the locations of the main detectors. I took the ADC (analog-to-digital converter) profiles from several runs and subtracted the profile from the negative half of the main detector bar from the profile from positive end, as shown in the top two plots from Figures 20 and 21. When it was properly normalized and with an increased number of bins in the histogram, I obtained histograms that looked like the bottom plots from Figures 20 and 21. The jump discontinuity in the exact center of the bar occurs because of the glue joint located there. When the two halves of the detector are subtracted, we obtain a histogram that begins negative and goes to the positive over the length of the entire detector bar. In my script I made a linear fit along the region of the jump discontinuity. Then, extracting the slope and vertical intercept from the fit, I calculated the horizontal intercept, which indicates the projected location of the glue joint in the main detector. We know that the glue joint should be at 0 cm, because the detectors are

made of two 1 m quartz bars glued together. Therefore, any deviation from that indicates that the vertical drift chambers were projecting the main detectors to a position different from the expected one.

After determining that my script was working properly, I ran it for a series of 5 runs, covering all eight octants and one reversed run. I obtained the location of the glue joint for each run and plotted the results versus octant. The resulting plot is found in Figure 22. We see a sinusoidal octant dependence in the first seven octants, which is, again, consistent with the VDC rotator being tilted at an angle. We do not know the reason for the outlier that occurred in octant 8, or why the reversed run points do not match the points from the normal run.

Next, I took four runs, all measuring in octants 1&5. However, in between the runs, the rotator was moved to a different set of octants to make some measurements and then was moved back to its original position. I ran this study to determine the reproducibility of the positioning of the vertical drift chambers, or whether the drift chambers returned to the same position after each rotation. I obtained the location of the glue joints for each of the runs, shown in Table 2, and plotted them versus run number; the resulting graph is shown in Figure 23. We see that there is some minor variation in the location of the center of the bar among the runs. This indicates that the drift chambers did not return to the exact same position each time it was rotated. However, there are no large variations which would have been a major problem for the precision of the position of the drift chambers.

Glue joint location, with rotation		
Run number	Octant 1 location (cm)	Octant 5 location (cm)
13665	2.4	-1.15
13681	2.29	-1.04
13688	2.27	-1.16
13723	2.36	-1.15

Table 2: Table of the glue joint locations (and, hence, the projected center of the main detector). The stability before and after rotations is decent, but there are some minor variations, indicating that the detectors were not positioned identically for all runs.

The final study that I ran was to examine the stability of the VDCs from run to run when the rotator was not deliberately moved. For this, I used a series of runs from a QTOR scan, in which only the current in the QTOR magnet was being varied. The drift chambers remained stationary

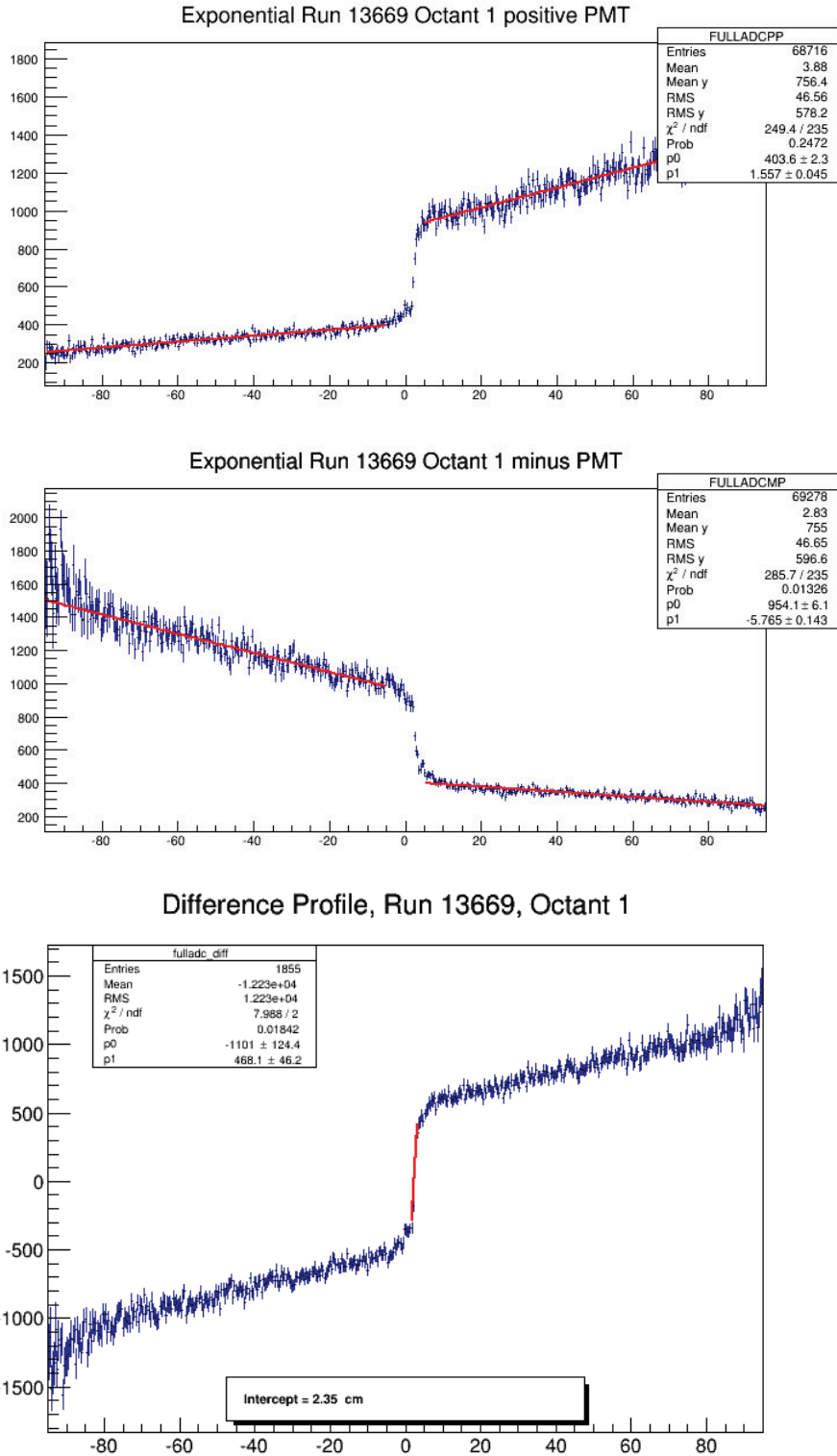


Figure 20: These plots show the ADC profiles for the octant 1 vertical drift chamber, when the rotator was positioned in octants 1 and 5. Because of the glue joint in the center of the bar, we see a jump discontinuity, which can be used to determine the relative positions of the detectors.

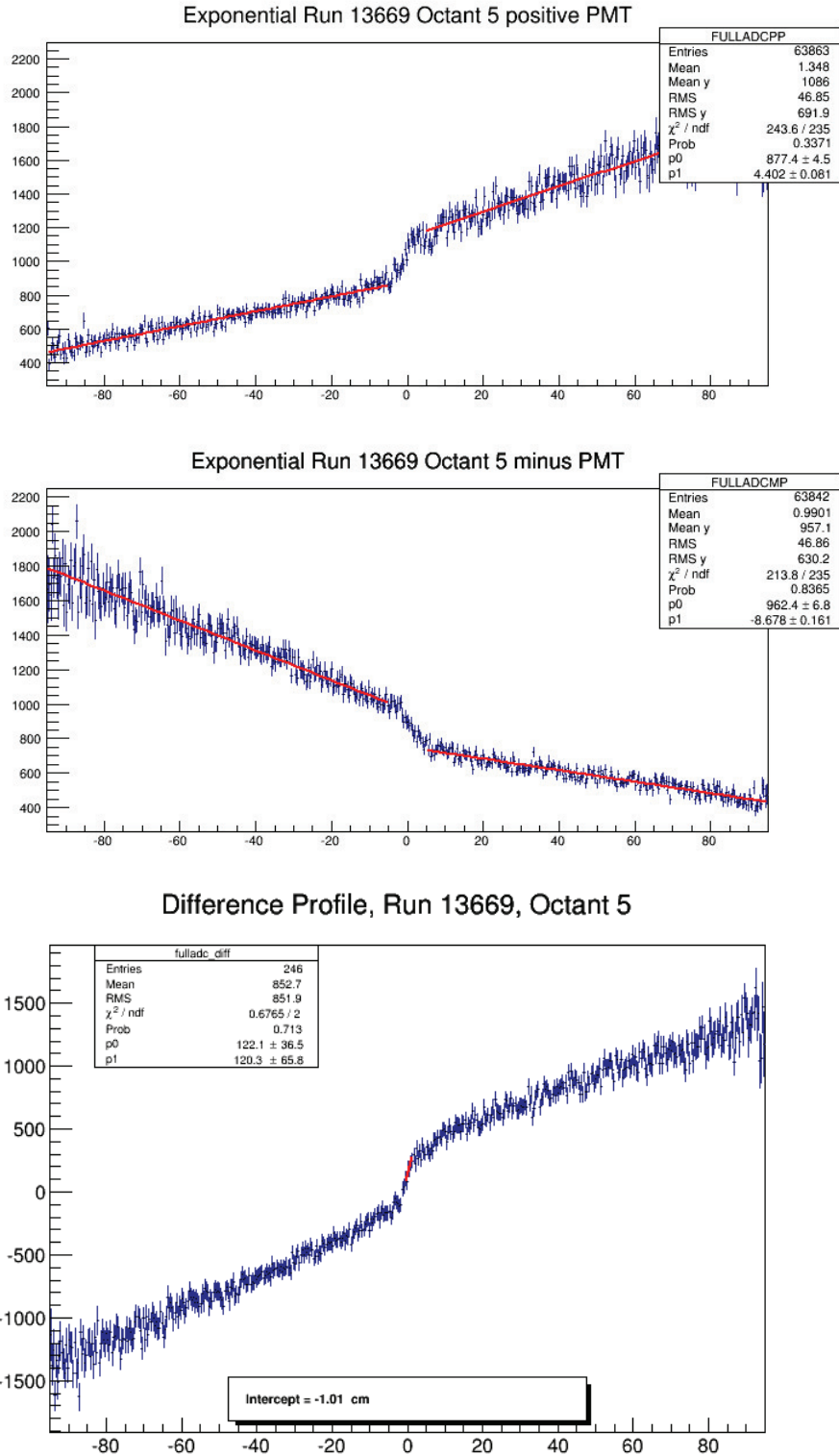


Figure 21: These plots show the ADC profiles for the octant 5 vertical drift chamber, when the rotator was positioned in octants 1 and 5. Because of the glue joint in the center of the bar, we see a jump discontinuity, which can be used to determine the relative positions of the detectors.

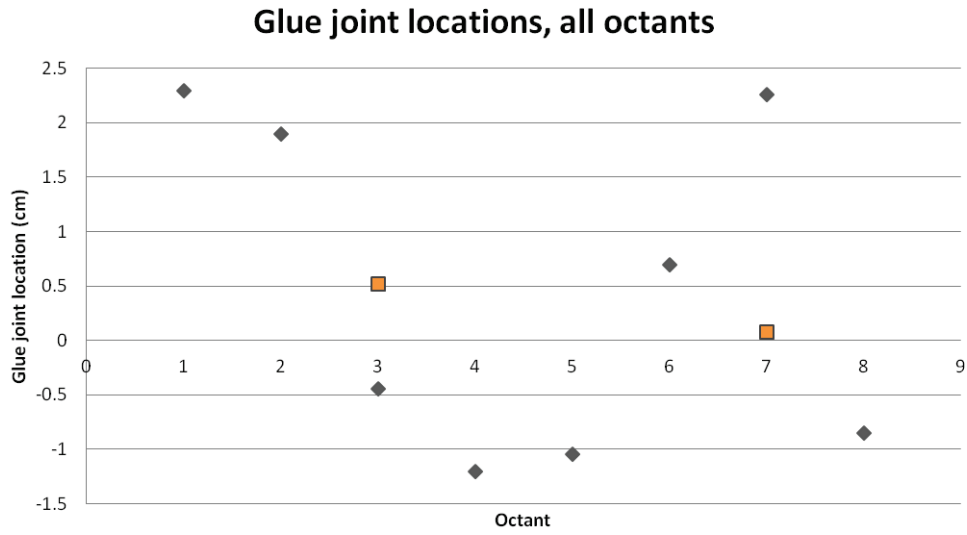


Figure 22: This plot shows the location of the glue joint for a set of five runs covering all eight octants with one reversed run (orange points). We see an octant dependence that appears to be sinusoidal, which is consistent with the hypothesis that the VDC rotator is tilted on its axis.

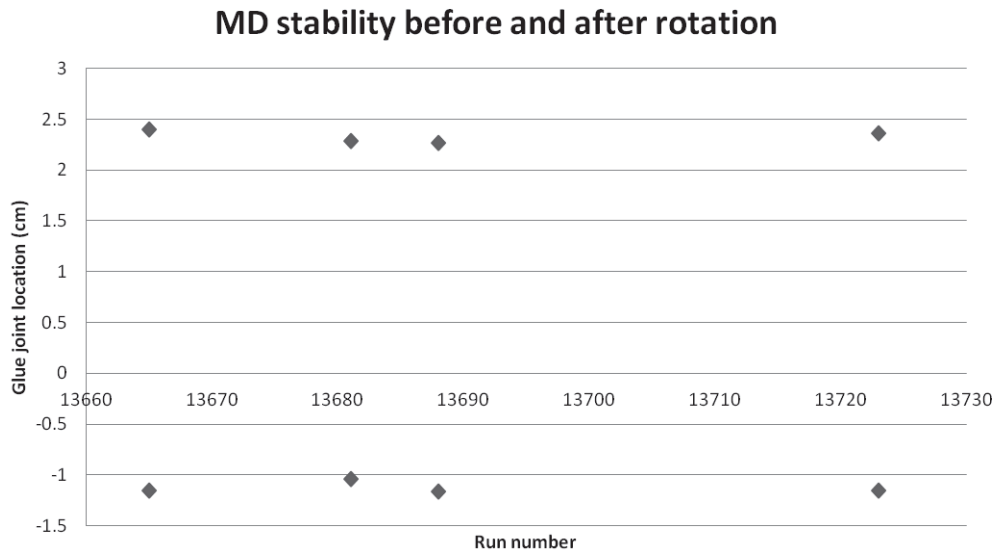


Figure 23: All of the runs in this set were measuring in octants 1 and 5. However, between some of the runs, the rotator was moved to a different set of octants and then brought back to the original position. This tests the reproducibility of the positioning of the drift chambers after rotation.

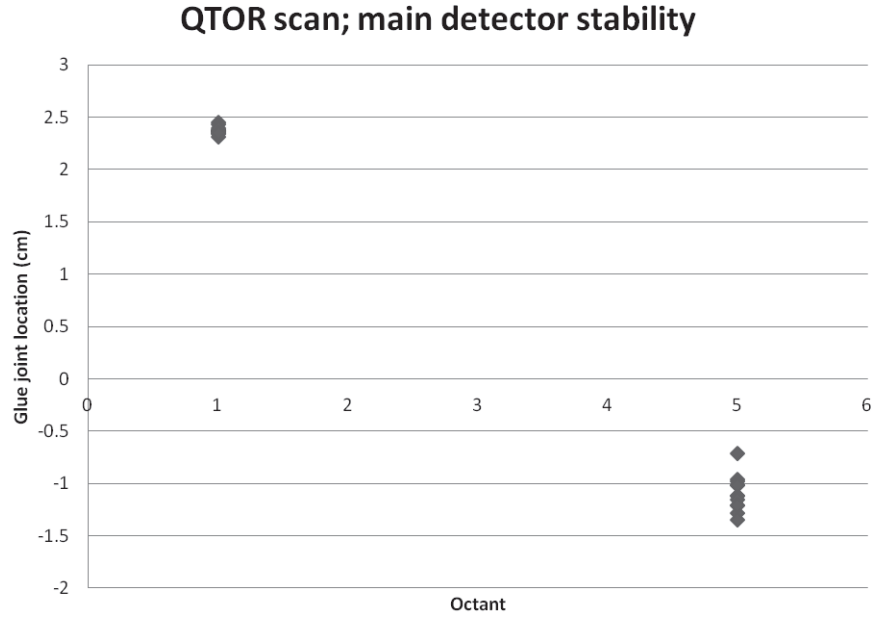


Figure 24: This figure shows a stability study. During the QTOR scan only the magnetic field was varied; the VDC rotator did not move. This examines the stability of the rotator from run to run.

in octants 1&5. I ran my script for the twelve runs in the scan, obtained the values for the location of the glue joint in each octant, and plotted these locations versus octant. The plot is shown in Figure 24. A table of the calculated locations of the center of the main detector is found in Table 3.

In Figures 23 and 24, I was examining the stability of the vertical drift chambers both when the rotator was being moved and when it was stationary. If the rotator were perfectly aligned, then we would have expected to find the location of the glue joints in the main detectors at exactly 0 cm. However, in the plots that I generated, the glue joint was consistently off-center, indicating that the rotator is probably tilted from the vertical. This explains the sinusoidal dependence with octant that we saw in Figure 22. In addition, it explains the results I have obtained for octants 1 and 5. Octant 1 is on the left side of the ring of the detectors and octant 5 is on the right right. See Figure 4 for reference.

Recall that the detectors have two photomultiplier tubes, one attached to each end. Because of the way that the geometry of the detectors was defined in the experiment, the “positive” end of the detectors is on the far end of the detector as one moves clockwise around the ring. These halves of the detector are denoted by a “+” in Figure 4. Knowing this geometry, we see that the

Glue joint location, with rotation

Run number	Octant 1 location (cm)	Octant 5 location (cm)
13658	2.45	-1.01
13659	2.37	-1.28
13660	2.38	-1.11
13661	2.36	-1.21
13662	2.38	-0.71
13663	2.37	-1.11
13664	2.44	-0.96
13665	2.40	-1.15
13666	2.34	-1.34
13667	2.32	-1.21
13668	2.35	-0.98
13669	2.35	-1.01

Table 3: Table of the glue joint locations (and, hence, the calculated center of the main detector) for the QTOR scan. The rotator did not move between runs for this sequence.

projected location of the center of the main detector being positive in octant 1 and negative in octant 5 is consistent with the VDC rotator being tilted backward on its axis. If the rotator is tilted backward, then the electron tracks will appear to be entering the main detectors at a higher point than they should have been. This translates to tracks being closer to the positive PMT in octant 1, and closer to the negative PMT in octant 5, which is what we have gathered from the data in Figures 23 and 24.

6 Conclusion

At the beginning of my project I found a discrepancy between the E' distribution from data and simulation. After trying many different tests to determine the reason for the anomaly, such as running different simulations to determine which energy loss processes are affecting the simulation or calculating the E' distribution using a different variable, we were able to determine the source of the problem with E' . By examining the octant-dependence of the mean value of E' and the locations of the main detectors as projected from the vertical drift chambers, we determined that the rotator upon which the vertical drift chambers are mounted was tilted at an angle from the vertical. The tilt was present in the physical experiment, but not in the simulation, explaining why we obtain a discrepancy between data and simulation.

The octant-dependent behavior of E' by octant is consistent with a tilt in the rotator. It now remains to determine the magnitude and direction of the tilt and alter the geometry in the simulation accordingly. Then, we will determine whether the distributions for E' , θ and Q^2 match between data and simulation to within the proper uncertainty. Finally, provided the distributions do match, a value for Q^2 will be extracted from the simulation and passed to the rest of the collaboration for the calculation of Q_{weak}^p .

When the final value for the weak charge of the proton is obtained, it can be used to calculate the weak mixing angle, θ_W , which is predicted by the Standard Model. If the values match, then the experiment will have verified the validity of the Standard Model and place limits on models that predict new physics. However, if the values do not match, then it would hint that there is physics beyond the Standard Model that has not been discovered yet. Of course, this type of experiment will have to be repeated in order to verify the results before any definitive conclusions are reached, but it will provide information about whether the Standard Model explains everything about the nature of particle physics, or whether there is new physics to be discovered.

References

- [1] "Standard Model." *Wikipedia: The Free Encyclopedia*. Wikimedia Foundation, Inc. 24 March 2014. Retrieved from http://en.wikipedia.org/wiki/Standard_Model
- [2] Qweak Collaboration. (2013). First Determination of the Weak Charge of the Proton *Phys. Rev. Lett*, 111(141083).
- [3] Erler, J., Kurylov, A., & Ramsey-Musolf, M. J. (2003). The Weak Charge of the Proton and New Physics *Phys. Rev. D*, 68(016006).
- [4] Leckey, J. P. (2008). *The First Direct Measurement of the Weak Charge of the Proton*. Retrieved from INSPIRE. (JLAB-PHY-12-1483)
- [5] Yang, S. (2013). *Title Unknown*. (Unpublished doctoral dissertation). College of William and Mary, Williamsburg, VA.
- [6] Qweak Collaboration Members. (2013, October 20). Qweak Wiki. Retrieved from https://qweak.jlab.org/wiki/index.php/Main_Page
- [7] Wang, P. (2010). QTOR Mapping and Main Detector for the Qweak Experiment. Paper presented at the Jlab Hall C Users Meeting, Newport News, VA.
- [8] Armstrong, D. (March 2013). Presentation at the Qweak Collaboration Meeting.
- [9] Armstrong, D. (March 2014). Presentation at the Qweak Collaboration Meeting, Washington D.C.
- [10] Armstrong, D. (2014). R3 projections to MD. Qweak Elog. Retrieved from <http://dilbert.physics.wm.edu/Physics/50>